Ocean Engineering 264 (2022) 112530

Contents lists available at ScienceDirect

Ocean Engineering

journal homepage: www.elsevier.com/locate/oceaneng

An investigation on the speed dependence of ice resistance using an advanced CFD+DEM approach based on pre-sawn ice tests

Luofeng Huang [a,*], Fang Li [b,**], Minghao Li [c], Danial Khojasteh [d], Zhenhua Luo [a], Pentti Kujala [b]

[a] School of Water, Energy and Environment, Cranfield University, UK
[b] Department of Mechanical Engineering, Aalto, University, Finland
[c] Department of Mechanics and Maritime Sciences, Chalmers University of Technology, Sweden
[d] School of Civil and Environmental Engineering, UNSW, Sydney, Australia

ARTICLE INFO

Keywords:
Polar ship
Pre-sawn ice
Ice resistance
Ice tank experiments
Computational fluid dynamics
Discrete element method

ABSTRACT

Over the past decades, the underlying mechanism of level ice resistance changing with ship speed has not been fully understood, particularly the resistance component due to ship interactions with broken ice pieces. Pre-sawn ice test can negate icebreaking component from the whole resistance of a ship in level ice, providing an effective approach to decompose ship-ice interactions and investigate the speed-dependent resistance from broken ice pieces. This work has built a computational model that can realistically simulate a ship advancing in a pre-sawn ice channel. The model applies Computational Fluid Dynamics (CFD) to solve the flow around an advancing ship, which is coupled with an enhanced Discrete Element Method (DEM) to model pre-sawn ice pieces. Model-scale experiments have also been conducted at the Aalto Ice Tank to validate the simulations, which shows the computational model can provide a reasonable estimation of the pre-sawn ice's resistance and movement around the ship. Upon validation, the dependence of ice resistance on ship speed was analysed. The simulations enable underwater monitoring of the ice motions, indicating that the speed dependence results from the mass of ice submerged underneath the ship and the displacement of broken ice induced by the ship. The identified relationships are more complex than the widely-used assumption that ice resistance linearly changes with ship speed in all cases, which provides a deeper understanding of ice resistance. As such, the findings from this study can potentially facilitate improvements in relevant empirical equations, useful for ship design, operational strategies and maritime management in polar regions.

1. Introduction

1.1. Speed dependence of ice resistance

Over the past decades, extensive laboratory and field tests have indicated that ice resistance generally increases with increasing ship speed (Spencer and Jones, 2001; Jeong et al., 2017, 2021; Zong et al., 2020; Gutiérrez-Romero et al., 2022). Though in certain conditions, ice resistance could also decrease or reveal no distinctive change with increasing ship speed, typically when the ship speed is not sufficiently high (Jones, 2004; Jeong et al., 2010; Suyuthi et al., 2011; Huang et al., 2016; Hu and Zhou, 2016; Yang et al., 2021). Yet, such a large number of observations have only led to empirical clues, and the underlying mechanism behind speed-dependent ice resistance has not been fully understood to date. In this context, relevant empirical equations and international guidelines still simplify a ship's ice resistance as linearly increasing with increasing ship speed (Lindqvist, 1989; Juva and Riska, 2002), although some tests did report strong non-linearity (van der Werff et al., 2015).

Ship-ice interactions are complex processes. For instance, ship advancement in level ice is a combination of breaking the ice sheet and then pushing away the broken ice pieces. Thus, the resistance involves components due to breaking the ice via crushing and bending (R_B), clearing the broken ice by displacing the ice pieces away (R_C), friction from ice pieces sliding along the hull (R_F), and pressure and viscous forces from water (R_{water}), which are required to be assessed separately (Lindqvist, 1989; Spencer and Jones, 2001; Jeong et al., 2010). There have been certain explanations for the speed dependence of R_B and

* Corresponding author.
** Corresponding author.
E-mail addresses: luofeng.huang@cranfield.ac.uk (L. Huang), fang.li@aalto.fi (F. Li).

https://doi.org/10.1016/j.oceaneng.2022.112530
Received 28 May 2022; Received in revised form 21 August 2022; Accepted 7 September 2022
Available online 18 September 2022

R_{water}. A higher ship velocity causes an ice sheet to withstand higher bending loads (Tan et al., 2014) and break into smaller sizes of ice pieces (Zhou et al., 2013), thus larger R_B; and a higher ship velocity induces larger viscous friction forces with water, thus larger R_{water}. However, the reasons for the speed dependence of ice resistance due to the interaction with broken ice pieces ($R_C + R_F$) are unclear. R_C is an inertial force due to the displacement of ice pieces, which has been assumed (in classic derivation) to be proportional to the ice mass that is being pushed. R_F is a frictional force generated from the submerged ice, which should be proportional to the ice mass underneath the ship. If the relevant ice mass was considered unchanged with varying ship speed, then both force terms would be independent of ship velocity. However, there has been clear evidence showing that R_C and R_F can significantly change with different ship speeds. This is proven by pre-sawn ice tests (ITTC, 2017), a standard experimental procedure to saw level ice following approximated breaking patterns and let the ship advance through. The pre-sawn ice tests exempt R_B thus the ship only bears R_C, R_F and R_{water}. By running accompanying tests without ice to ascertain R_{water}, the sum of R_C and R_F can be obtained. Test results have shown that R_C and R_F certainly change with varying ship speed, but the underlying mechanism requires to be explained (Spencer and Jones, 2001; ITTC, 2002).

One of the earliest investigation into the speed dependence of ice resistance was carried out by Enkvist (1972), which analysed several possible sources of speed dependence, including downward acceleration of ice pieces, dynamics pressure, and turning of broken ice pieces. Through analytical calculations, Enkvist (1972) concluded that the speed dependence is majorly attributed to the turning of ice pieces after being broken off from the intact ice sheet. The fast turning of ice pieces results in the so-called "ventilation effect" where a no-water zone forms above the ice piece, which increases the force from water acting on the ice piece and hence the resistance grows. The ventilation effect was then more systematically investigated by Valanto (1989, 2001) with both experiments and numerical solutions. His work showed that the resistance due to the turning of ice pieces is considerable, but the speed dependence is not evident, e.g. referring to Figure 24 in (Valanto, 2001). The exclusion of ice turning as a source of speed dependence is supported by Kämäräinen (1993) based on theoretical analysis and full-scale measurements. More recently, the ventilation effect was numerically investigated by Lu et al. (2012), who found that, while ventilation plays an important role in the process, the assumption of full ventilation, as adopted by Enkvist (1972), can lead to overestimation of the resistance. The resistance due to the turning of ice floe was taken into account by Li et al. (2021) in their ship performance simulation model through a simplified approach. The resistance due to the turning of ice floe was found to account for less than 20% of the total ice resistance. Overall, the existing literature indicates that it remains largely debatable whether the turning of ice pieces is a major source of speed dependence.

While excluding ice turning as the source of speed dependence, Kämäräinen (1993) regarded the submerging of ice as the major contributor to speed dependence. He noted that the nature of hull-ice contact in the submersion phase was an unexplored subject at that time. Alternatively, he presented an analysis of the process which supported the pressure change between the submerged ice piece and ship hull, which addresses the speed dependence but not comprehensively. The phenomenon of pressure change was then experimentally observed by Puntigliano Etchart (2003). Following that, Kämäräinen (2007) continued the investigation by CFD simulation of the gap between an ice piece and ship hull. He concluded that the force resulting from a pressure decrease in the gap may be several times higher than the force resulting from the static lift of the ice floes. However, a measurement to confirm such an effect is still missing, and succeeding investigations of this phenomenon have not been reported.

A holistic view of the overall ice piece distribution and motion is still missing. Such insights can be obtained by analysing underwater images of ships going through level ice or pre-sawn ice. However, existing pre-sawn ice tests did not perform systematic image analysis of the underwater ice piece distribution. Myland and Ehlers (2020) ran four ship models through level ice with different speeds and thicknesses and investigated the ice coverage via image analysis, but the results did not reveal clear dependence of ice coverage on ship speed. Further experimental investigations are lacking due to the costs of copious runs required plus the manufacturing and sawing of ice sheets that may take one or two days for each run. Moreover, the experimental measurement in pre-sawn ice tests is the sum of R_C and R_F, which does not provide more insights into the ship-ice interactions. Computational simulation provides an alternative method which is cost-effective and makes it possible for detailed analysis of the interactions. As reviewed by Li and Huang (2022), pre-sawn ice simulations are rare in the literature. Two works have been found (Konno and Mizuki, 2006; Sawamura et al., 2015) adopting a physically based modelling approach considering the contact as an impulse and simplifying the fluid force by empirical drag. The ships were set to go through pre-sawn ice and the resistance and ice patterns were analysed. However, no results related to the speed dependence were presented.

1.2. Scope and novelty of this paper

Simulation through combined CFD + DEM modelling is promising to investigate ship-ice interactions, and this has been demonstrated in ice-floe and brash-ice conditions (Mucha, 2019; Huang et al., 2020; Luo et al., 2020). It is deemed that this approach has the potential to accurately model broken ice pieces from the icebreaking process, which may help identify the relationship between ice resistance and varying ship speed. In this context, the present study develops a CFD + DEM model to simulate the ship interaction with pre-sawn ice. As the ice motions around a ship are particularly important for analysing the speed dependence of ice resistance, the previous modelling approach in (Huang et al., 2020), by modelling an ice floe as only one DEM element, is no longer capable. To enable accurately modelling of pre-sawn ice tests, an improvement for the DEM part is implemented in this work, modelling each ice floe by multiple number of DEM elements. In addition, parallel experimental tests were carried out simultaneously at the Aalto Ice Tank to validate the enhanced model. Based on the CFD + DEM model, a series of computational studies are performed, providing key information on the ship-ice interaction, such as the movement of ice blocks underneath the ship. The investigation through CFD + DEM simulation specifically aims to answer one research question: how does speed affect the ice piece distribution and motion around a ship thus the ice resistance? This is for the first time that analyses are conducted to present insights into the speed dependence of R_C and R_F.

2. Computational approach

2.1. Computational domain and boundary conditions

Using the STAR-CCM + software, a three-dimensional rectangular computational domain was established, with the lower part filled with water and the upper part filled with air. A hull was placed between two large ice sheets to form an open-water ice channel (Huang et al., 2021a). The applied ship model, named "Infuture", is a double-acting river-sea going vessel that has an open water bow combined with an icebreaking stern, thereby operating astern during independent navigation in ice.

Table 1
Particulars of the applied ship model.

	Full-scale	Model-scale
Length overall (m)	92.5	5.50
Breadth (m)	12.6	0.75
Depth (m)	8	0.48
Draught (m)	4.45	0.26
Displacement (ton)	4053	0.852

The main parameters of the ship model are given in Table 1. Model scale is applied in the computational model, which is for the purpose of validation against experiments, and the scaling factor is 16.8.

The water path in front of the ship was covered by parallelogram-shaped pre-sawn ice as usually adopted in model scale tests (ITTC, 2017). The initial condition of the simulation is depicted in Fig. 1, and the shape of the ice floe is depicted in Fig. 2. The side boundaries are half a ship length from the ship's centre plane, which is enough to avoid undesired wave reflection by the boundaries as the ice sheets will damp the wave radiation. The top and bottom boundaries are also half a ship length away from the ship, both have negligible influence on the ship hydrodynamics. The top is set as pressure outlet to model atmosphere, and other boundaries are set as wall to model an ice tank.

The ship-water hydrodynamics were solved by CFD, while the pre-sawn ice was modelled by DEM. One-way coupling between CFD and DEM was used to save computational resources, as previous studies suggested that using two-way coupling would not notably change the results when simulating ship-ice interactions (Mucha, 2019; Luo et al., 2020). As pre-sawn ice tests normally do not induce ice bending or crushing, the ship and ice were modelled as rigid bodies. Each pre-sawn ice piece was modelled by an amount of DEM particles clumped together, as shown in the close-up view of Fig. 1. 175/75/35 particles respectively were used to construct each pre-sawn ice block with 24/36/48 mm thickness, as shown in Fig. 3. The number of particles is determined based on the ice block's thickness and surface area - since each particle is spherical, for the same surface area, thinner ice requires more particles. In order to meet the shape requirement, the used particle numbers are not flexible. However, the particle numbers do not influence the solution so long as the desired shape is constructed, which is because each ice block is still treated as a whole rigid body to obtain its motion solution.

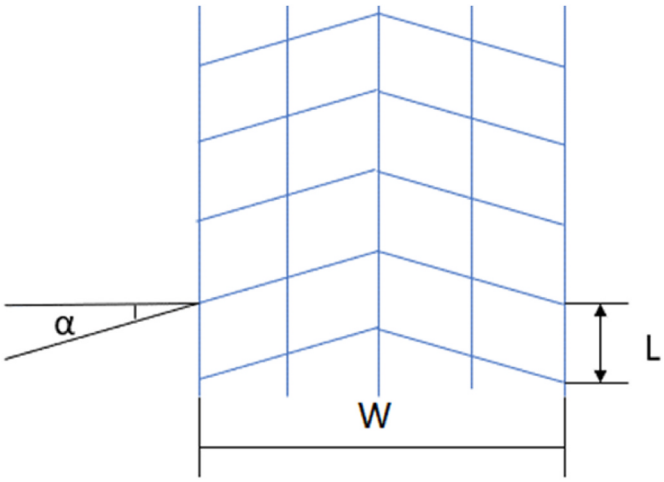

Fig. 2. Sketch of pre-sawn ice pattern, where L = 0.20 m, W = 0.85m and α = 10°..

This treatment enabled an improved computational fidelity than previous work using only one DEM particle for one ice block (Huang et al., 2020). With this treatment, each DEM particle obtains its own CFD solution from the transient particular location. Thus, the motion of an ice piece results from the integration of numerous particles. The essential enhancement here is the ability to accurately solve the rotational motion of each ice block, because using only one DEM particle for one ice piece revealed unphysical rotations. It is impossible for a

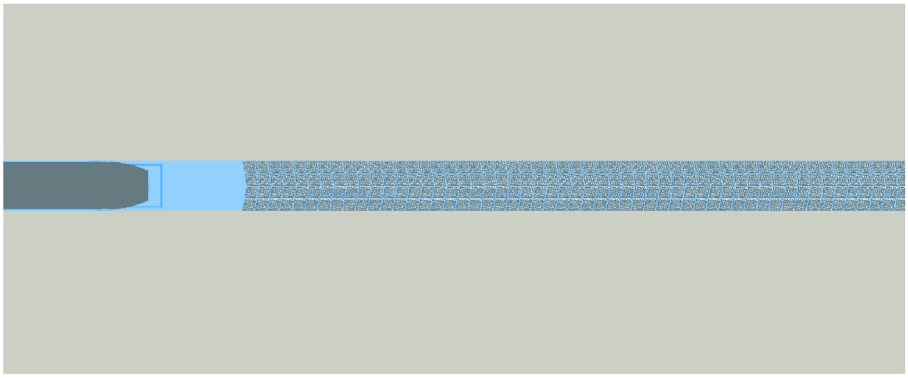

(a) overall view

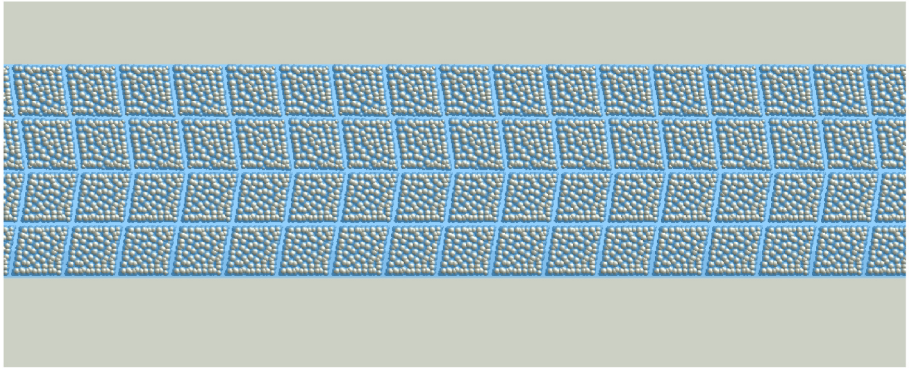

(b) close-up view of the pre-sawn ice modelled by high-resolution DEM particles

Fig. 1. Initialisation of the computational model.

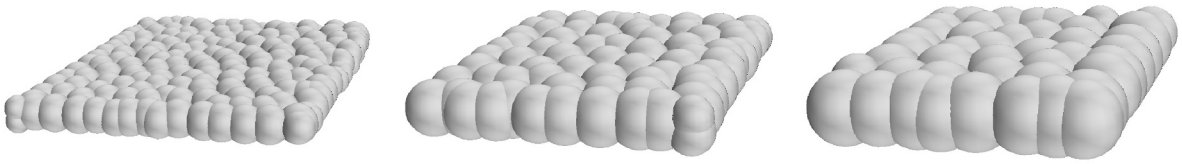

(a) h = 24 mm (b) h = 36 mm (c) h = 48 mm

Fig. 3. Models for different thicknesses of ice floes.

single-particle ice floe to have reasonable rotations, because there is only one solution point (at the gravity centre of the particle), while multiple solution points (between the gravity centre and edges) for one ice floe are required to accurately calculate torque which is essential for solving rotational motions. In addition, the single-element approach might limit the ice shape within those that have existing DEM solutions, e.g. disk and sphere. The present multiple-clumped-elements approach can facilitate arbitrary shapes of ice floes. A realistic match between simulated ice shape and real ice shape may be achieved through the method introduced in Huang et al. (2022). Nonetheless, the previous single-particle approach was found capable of predicting the integral resistance as well as the fuel consumption of a ship operating in ice floes (Huang et al., 2021b). Seo and Wang (2021) applied the single-particle CFD + DEM approach to simulate a ship advancing in pre-sawn ice, presenting good agreement with experiments regarding the resistance, but did not show sufficient justification on the accuracy of ice floes' rotations. The ice resistance could be accurately predicted using the single-particle DEM approach as the force is mainly related to translational motions. This multiple-particle DEM approach has been used by Zhang et al. (2022) to simulate a ship advancing in brash ice. The present work is first time for the approach to be applied to the pre-sawn ice scenario. Noting that the ice shape and rotational motions matters much more for the pre-sawn case than the brash-ice case, the importance of applying the advanced CFD + DEM approach in the present work is justified.

Once the simulation starts, the ship is set to advance in pre-sawn ice for two ship lengths, with a fixed velocity. The ship advancement was achieved through an overset mesh approach. The overset approach is essential in the present case as the ship moves a large distance in the domain, which would distort the fluid mesh and cause simulation crashing if a conventional dynamic-mesh approach was used. More details for the overset mesh treatment have been introduced in Huang et al. (2021c).

2.2. Governing equations

The CFD fluid flow was solved by the standard Reynolds-averaged Navier-Stokes (RANS) equations:

$$\nabla \cdot \bar{\mathbf{v}} = 0 \tag{1}$$

$$\frac{\partial(\rho\bar{\mathbf{v}})}{\partial t} + \nabla \cdot (\rho\bar{\mathbf{v}}\bar{\mathbf{v}}) = -\nabla\bar{p} + \nabla \cdot (\bar{\tau} - \rho\overline{\mathbf{v}'\mathbf{v}'}) + \rho g \tag{2}$$

where $\bar{\mathbf{v}}$ is the time-averaged velocity, $\mathbf{v}'$ is the velocity fluctuation, ρ is the fluid density, $\bar{p}$ denotes the time-averaged pressure, $\bar{\tau} = \mu[\nabla \mathrm{v} + (\nabla \mathrm{v})^{\mathrm{T}}]$ is the viscous stress term, μ is the dynamic viscosity and g is gravitational acceleration set at 9.81 m/s^2. Since the RANS equations have considered the turbulent fluid, the Shear Stress Transport (SST) k − ω model (Menter, 1993) was adopted to close the equations. Pena and Huang (2021) reviewed a large volume of CFD works in ship hydrodynamics, in which different options of turbulence models were compared. The review indicates that the SST k − ω model has been widely validated as an appropriate turbulence model for ship flows. Nonetheless, other RANS models may also be valid choices as their accuracy is at the same level as SST k – ω (Terziev et al., 2019).

The free surface between the air and water was modelled by the Volume of Fluid (VOF) method (Hirt and Nichols, 1981). The VOF method introduces a passive scalar β, denoting the fractional volume of a cell occupied by a specific phase. In this case, a value of $\beta = 1$ corresponds to a cell full of water and a value of $\beta = 0$ indicates a cell full of air. Thus, the free surface, which is a mix of these two phases, is formed by the cells with $0 < \beta < 1$. The elevation of the free surface along time is obtained by the advection equation of β, expressed as Equation (3). For a cell containing both air and water, its density and viscosity are determined by a linear average according to Equation (4) and Equation (5). In this study, $\rho_{\mathrm{water}} = 998.8$ kg/m^3, $\mu_{\mathrm{water}} = 8.90 \times 10^{-4}$ N s/m^2; $\rho_{\mathrm{air}} = 1$ kg/m^3, $\mu_{\mathrm{air}} = 1.48 \times 10^{-5}$ N s/m^2.

$$\frac{\partial\beta}{\partial t} + \nabla \cdot (\bar{\mathbf{v}}\alpha) = 0 \tag{3}$$

$$\rho = \beta\rho_{water} + (1-\beta)\rho_{air} \tag{4}$$

$$\mu = \beta\mu_{water} + (1-\beta)\mu_{air} \tag{5}$$

Each pre-sawn ice piece has its own Lagrangian reference frame, moving in the Eulerian CFD domain (Baran, 2012). The movement can be considered as the combination of translation and rotation, which was solved with the rigid-body motion equations in the body-fixed system based on the mass centre of the floe G–$x'y'z'$:

$$\mathbf{F} = m\frac{d\overrightarrow{V_G}}{dt} \tag{6}$$

$$\mathbf{T} = [\mathrm{J}] \cdot \frac{d\overrightarrow{\omega_G}}{dt} + \overrightarrow{\omega_G} \times ([J] \cdot \overrightarrow{\omega_G}) \tag{7}$$

where **F** and **T** are the total force and torque on the ice floe, induced by the gravity, the hydraulic load from the surrounding fluid $\mathbf{F_h}$ and the contact force **Fc** from ship-ice contact and ice-ice contact; m and [J] are the mass and inertia moment tensor respectively, and $\mathrm{V_G}$ and ω_G are respectively the translational and rotational velocity vectors of the ice piece.

As introduced in Section 2.1 the hydraulic force $\mathbf{F_h}$ on an ice piece is the integrated CFD force of its all particles. Similarly, the contact force $\mathbf{F_c}$ is an integrated solution from each particle's transient contact. The contact was solved by a penalty method (Cundall and Strack, 1979), where potential ship-ice or ice-ice contacts are allowed to have a temporary overlap, as if the two colliding bodies penetrate each other following the transient motion status. The overlap then generates a force to push the overlapping particles away. As a result, the overlap is gradually minimised along each DEM timestep, while the contact force is recorded. The contact force is calculated using the Hertz-Mindlin approach (Johnson and Johnson, 1987), which is a spring-dashpot system where the spring (k) accounts for the elastic response and the dashpot (η) reflects the energy dissipation. The normal and tangential components of $\mathbf{F_c}$ are calculated according to Equations 8–11.

$$\mathbf{F_n} = -k_n d_n - \eta v_n \tag{8}$$

$$\mathbf{F}_t = \begin{cases} -k_t d_t - \eta v_t \ , \ if \ |d_t| < |d_n| \mathrm{C}_f \\ |k_t d_n| \mathrm{C}_f \cdot n \ , \ if \ |d_t| \geq |d_n| \mathrm{C}_f \end{cases} \tag{9}$$

$$k_n = 3/4 E_{eq} \sqrt{d_n R_{eq}} \tag{10}$$

$$k_t = 8 G_{eq} \sqrt{d_t R_{eq}} \tag{11}$$

where d_n and d_t are overlap distances in the normal and tangential directions respectively, v_n and v_t are the normal and tangential components of the relative velocity between two contact bodies, and $\mathrm{C_f}$ is the friction coefficient. E, G and R are respectively Young's Modulus, Shear Modulus and Radius, where the subscript eq denotes the equivalent value from the two contact bodies, e.g. $R_{eq} = R_A R_B / (R_A + R_B)$. η was set at 0.6 in this study, which is an empirical value that can be used to calibrate the simulations to maximise the consistency between the physical and simulated ship-ice interactions.

2.3. Mesh sensitivity study

In order to solve the governing equations, the computational domain was discretised using the Finite Volume Method (Versteeg and Malalasekera, 2007). The meshing approach is presented in Fig. 4. The cell shape is based on cubic while the shape may change in particular regions, e.g. due to the curvature of the hull. The domain was discretised using a base size ($d = \Delta x = \Delta y = \Delta z$). Special mesh treatments are required for this particular case: (a) 16 layers of mesh is applied around the hull as well as between the hull and the ice sheets to capture the boundary layer effect the layer thickness is $1/20d$; (b) expected ship-floe interaction regions are refined, i.e. in front and below the hull, and free surface region is refined the refined cell size is $1/10d$.

As the computational cost increases with the cell number, a mesh sensitivity study was conducted in order to get a reliable solution with as few cells as possible. Since CFD is Eulerian and DEM is Lagrangian, only the CFD (i.e. the fluid part) consists of cells. Therefore, the model was

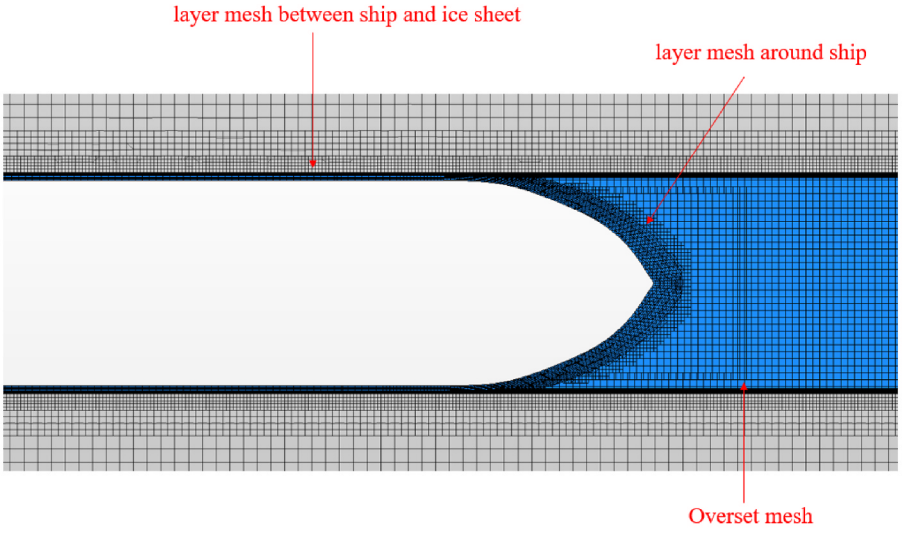

(a) Plan view

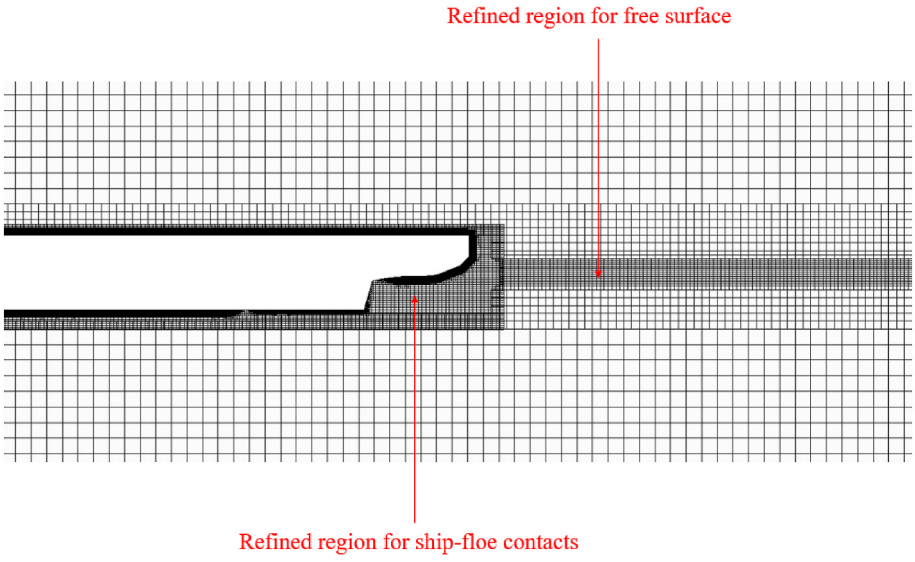

(b) Profile view

Fig. 4. Mesh layout of the model.

examined without DEM ice floes and R_{water} on the ship was selected as the parameter to analyse mesh convergency. For the sensitivity study, d was varid as $d_1 = 0.165\ m$, $d_2 = 0.125\ m$, $d_3 = 0.1\ m$, $d_4 = 0.075\ m$, and four sets of mesh were produced, respectively having a cell number of 1.49, 2.65, 4.36 and 8.32 million. The four sets of mesh were tested with the ship advancing at V = 0.488 m/s and between h = 36 mm thick ice sheets.

The size of each timestep was determined by a prescribed Courant number (Co) value, according to the expression:

$$\mathrm{Co} = \frac{v_n \Delta t}{d} \tag{12}$$

where Δt denotes the time step size, v_n is the flux speed through the shared face between two neighbouring cells, and Δx is its distance between the centres of the two cells. Co is limited to be smaller than 1 which is a standard of ship hydrodynamic CFD (ITTC, 2014). Based on this index, the timestep size is automatically varied according to the tested cell size.

The results of the mesh sensitivity study is presented Fig. 5. It can be seen that the water resistance converges with the cell number increased, while the improvement between 4.36 million cells and 8.32 million cells is not distinct. Therefore, the mesh with 4.36 million cells was selected to conduct the following analyses, as there is no need to use a higher cell number. This corresponds to a computational time of approximately 48 h using 120 processors.

3. Validation

3.1. Ice tank experiments

To confirm the validity of the proposed CFD + DEM approach, pre-sawn ice tests of a ship advancing in pre-sawn ice were conducted at the Aalto Ice Tank. Information of the ship has been presented in Section 2.1. The tests in pre-sawn ice were prepared according to the ITTC guidelines for ice model tests (ITTC, 2017). Fine-grained model ice was produced by spraying layers of ethanol doped mist over several hours to achieve the desired thickness and strength. A drill was first fixed to the carriage to cut the gaps along the towing direction, and then held manually to saw the oblique pattern. The channels were wider than the ship model by 2–3 times the ice thickness in accordance with the ITTC guideline. The angle of cutting was kept at 10° which is close to the ship waterline angle, so that the pre-sawn ice approximated the breaking pattern (ITTC, 2017). This yielded parallelogram ice pieces approximately 20 cm long and 21.25 cm wide (a quarter of the channel width), as depicted in Fig. 2. Fig. 6 presents the experimental setup. The ice thicknesses are set to 24 mm and 36 mm in model scale, i.e. 40 cm and 60 cm in full-scale, as the ship was design to break up to 60 cm ice.

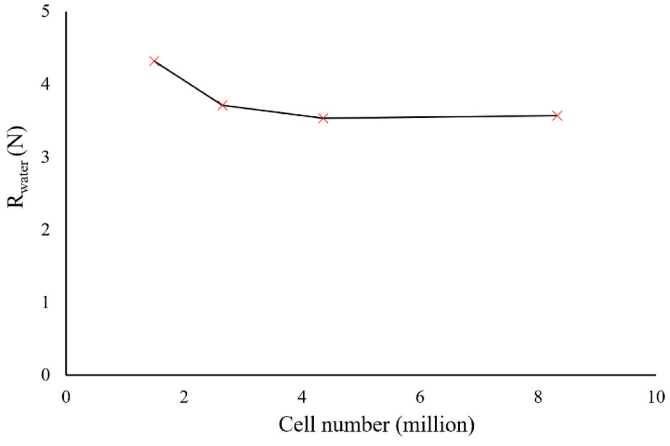

Fig. 5. Water resistance of the ship as a function of cell number (V = 0.488 m/s).

The pre-sawn ice tests included four runs: (a) the first two runs towed the ship in pre-sawn ice with different ice thicknesses and ship velocities, and (b) the next two runs removed pre-sawn ice and then towed the ship through the open-water ice channel to measure the resistance from water. The test details are given in Table 2. These tests were carried out without a propulsion unit thus representing resistance on the bare hull. The resistance was measured through towing tests. Before each test, the model ship was placed close to the pre-sawn ice channel, and the centreline of the model ship was aligned with the middle of the ice pieces. During the towing process, the resistance was measured with a load sensor, which was connected to the model via a shackle-shackle connection that can enhance the stability. The ship model was fixed to the towed carriage right below the carriage, and was towed by the carriage via a towing wire. A counterweight was applied to tighten the wire and damp the possible surging motions during the tests. The sway and yaw motions were restricted by two guiding posts, so the heading of the ship was kept aligned with the channel. The carriage was set to move at the target speeds, thereby towing the ship model through ice. Fig. 7 gives an example of the measured towing force and the extraction of ice resistance.

The ice thickness and mechanical properties were measured in-situ at multiple locations of the ice. The average values of the measurements are presented in Table 2. Although measured, the strength properties are not required for the simulations presented later, as the ice blocks behaved as rigid bodies in the pre-sawn ice tests. The dynamic friction coefficient between the ship and ice was measured ex-situ by moving an ice sample along the wetted ship surface. A deadweight of 2 kg and a wooden plate were placed above the ice sample after weighing. The required force was measured with a load sensor to determine the friction coefficient. In total, three frictional tests were conducted, yielding an average friction coefficient of 0.085 with negligible variations between tests.

3.2. Comparison between simulations and experiments

Simulations were performed to replicate the experimental tests. Fig. 8 presents a simulation when the ship is advancing in pre-sawn ice, showing both bird and fish views. It can be seen that ship-ice collisions occur at the front area, causing the pre-sawn ice to be pushed aside and underneath the ship. In general, the outer two columns of ice pieces are mostly pushed underneath the level ice sheets, while the middle two columns of ice pieces are displaced to slide underneath the ship. The simulated movement of ice pieces is very similar to that observed in experiments, as shown in Fig. 9. This figure also shows that the ice pieces mostly remain intact after the interaction with the ship, which supports the rigid body assumption adopted to model the ice.

The total resistance of the ship in pre-sawn ice consists of an ice resistance R_{ice} and a water resistance R_{water} ($R_{total} = R_{ice} + R_{water}$), in which R_{ice} is the sum of R_C and R_F. The time-series R_{ice} recorded from simulations is shown in Fig. 10. Effective resistance data were taken only when the resistance becomes relatively stable, where the resistance still oscillates (because the simulation is transient) but its average value does not change notably, as indicated by a green-dash box in Fig. 10. This corresponds to the status that the ship has sufficiently entered the ice field.

A comparison is drawn between the computational and experimental resistance data, as presented in Table 3. For computational results, R_{ice} and R_{water} are automatically separated by the DEM and CFD solvers; for experimental results, R_{ice} is calculated as the resistance from Test 1.1/2.1 minus those of Test 1.2/2.2 (Table 2).

It can be seen that the computational and experimental results agree well with each other. Deviations are less than 10%, except for R_{water} of Test 1.2. This discrepancy in R_{water} should attribute to experimental uncertainty due to the large measuring range of the load sensor (500 N), which becomes inaccurate when measuring very small forces, e.g. the

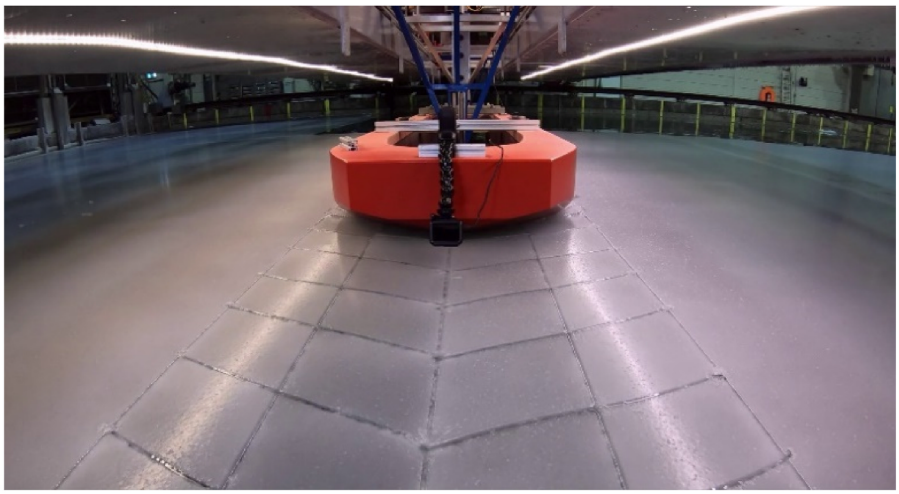

(a) Front view

(b) Side view

Fig. 6. The ship model being towed through pre-sawn ice (h = 36 mm).

Table 2
Measurements from the experiments, where h is pre-sawn ice thickness, V is ship speed, σ_f is flexural strength, E is Young's Modules and R is total resistance.

Test	h (mm)	V (m/s)	σ_f (kPa)	E (MPa)	R (N)
1.1	24	0.244	48.9	156.3	12.65
1.2	–	0.244	–	–	0.46
2.1	36	0.488	43.0	83.6	32.76
2.2	–	0.488	–	–	3.53

measured R_{water} of 0.46 N has the same order of magnitude as the sensor's uncertainty. Such measurement uncertainty however has negligible influence on the comparison of R_{ice}, as its magnitude is much larger than the noise level. Based on the validation of both ice motions and ship resistance, the built CFD + DEM model is shown to reasonably replicate the pre-sawn ice experiments.

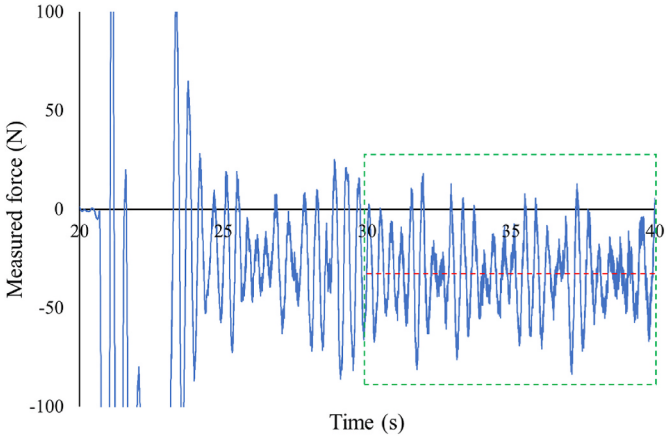

Fig. 7. Time history of the towing force of Test 2.1; green box indicates the stable period and red dashed line shows the average foce

4. Influence of ship speed on ice resistance

4.1. Simulation results

Upon the validation of the CFD + DEM approach, systematic

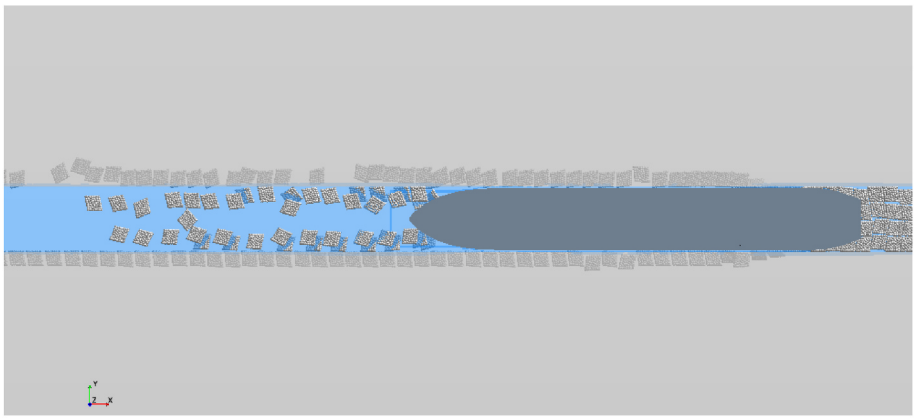

(a) Bird view

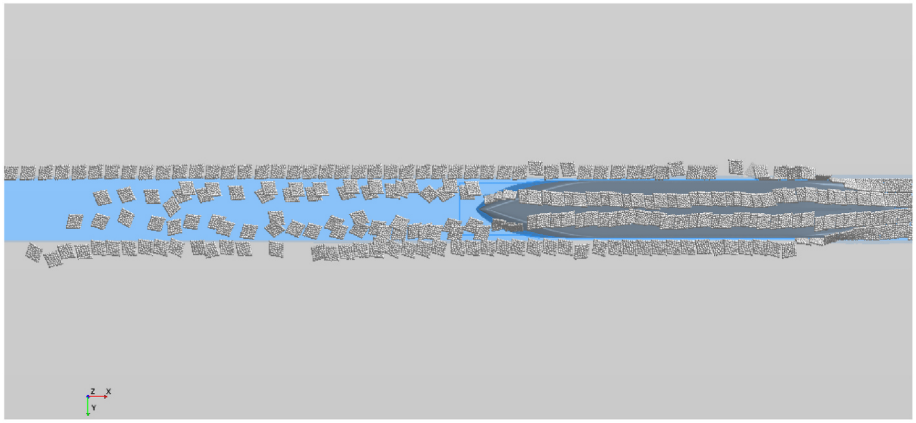

(b) Fish view

Fig. 8. Simulation of a ship advancing in pre-sawn ice (h = 36 mm, V = 0.488 m/s).

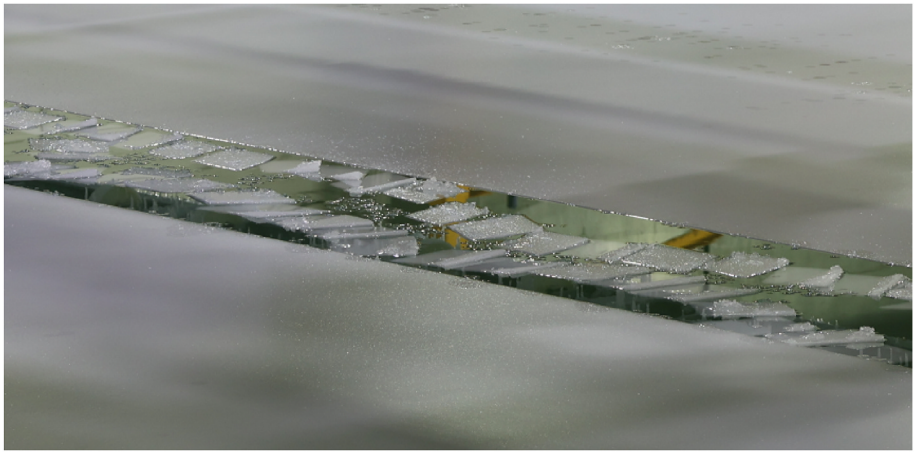

Fig. 9. Experimental observation of ice layout after the ship went through – middle two columns are left in the open-water ice channels and the outer two columns are hidden under level ice sheets (h = 36 mm, V = 0.488 m/s).

simulations were conducted to investigate the ice resistance change at different ship speeds and at different ice thickness conditions. The focus is to see how varying ship speed changes the ice piece distribution and movement and thereby affects the resistance. This is because ice piece distribution and movement are key for R_C and R_F. For this aim, the surface area of ice pieces was remained constant and ship speed is changed at different ice thicknesses. Systematic simulations were conducted for a range of ship speeds varying from V = 0.244 m/s to 1.464 m/s (Froude number, Fr = 0.033–0.2). Three ice thickness conditions (h = 24, 36, and 48 mm) were employed as a test matrix against different ship speeds. The computational results are presented in Fig. 11.

For the lowest ice thickness tested, h = 24 mm, a nearly linear

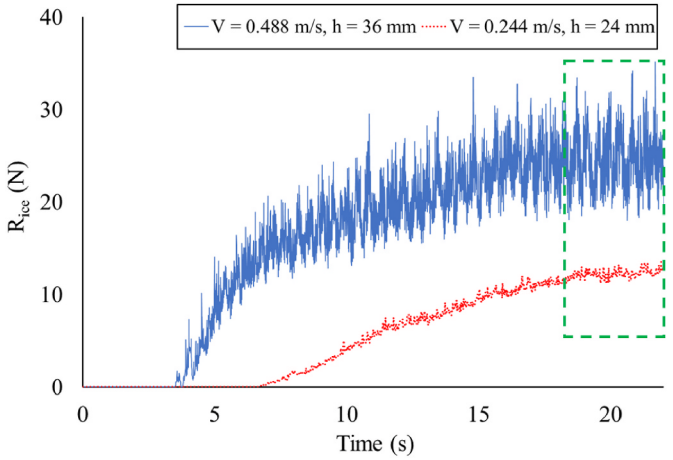

Fig. 10. Time-series R_{ice} from simulations. The green-dash box indicates the data used to calculate the averaged resistance results. (For interpretation of the references to colour in this figure legend, the reader is referred to the Web version of this article.)

Table 3
Comparison between experimental and computational results.

	Experimental (N)	Computational (N)	Deviation
Test 1.1, R_{ice}	12.21	12.18	−0.24%
Test 1.2, R_{water}	0.46	1.00	+117%
Test 2.1, R_{ice}	29.23	26.88	−8.04%
Test 2.2, R_{water}	3.53	3.24	−8.21%

relationship is observed. To investigate the reason for the resistance to change, the underwater ship-ice interaction is analysed. As shown in Fig. 12, the Number of Submerged Ice Blocks (NSIB) is counted and each ice block's perpendicular distance to the ship centreline is presented. An ice floe is deemed as NSIB if its 80% surface area is under the hull. The NSIB is responsible for the frictional part, i.e. R_F, whilst the perpendicular distance indicates how far the ship has pushed the ice blocks away, which results from R_C that provides the kinetic energy.

It can be seen between Fig. 12(a) and (b) that the under-ship ice shows a uniformly-distributed pattern and the NSIB remains unchanged between Fr = 0.066 and 0.133, which means R_F does not change. Thus, the slightly increased resistance results from R_C, as the ice blocks are displaced more for Fr = 0.133 than Fr = 0.066. This can be observed from the middle two columns of ice, which are more diverged from the centreline in Fig. 12(b) than in Fig. 12(a), indicating more kinetic energy gained through the ship-ice interaction thus the ice blocks drifted further away. When Fr is equal to 0.2, although NSIB has decreased, the uniform underwater pattern has been broken. The ice blocks' distribution is chaotic and their displacements are much larger than those observed for lower speeds, as per Fig. 12(c). This induces much higher R_C and an overall higher R_{ice}, despite a decreased R_F component. Overall, a trend can be seen as increasing ship speed decreases R_F and increases R_C, whilst the change in R_C is larger than the change in R_F.

Results with h = 36 mm and 48 mm show a stronge non-linearity. The resistance changes very little when the speed is relatively low but grows extensively in the high-speed regime. For h = 36 mm, it can be seen in Fig. 13(a) and (b) that the underwater ice patterns are alike between Fr = 0.066 and 0.133, while the NSIB of Fr = 0.066 is higher as ice blocks overlap each other due to a lower ship speed. The resistance does not exhibit a distinctive change in this speed range, which indicates that the changes in R_F and R_C approximately offset each other in these conditions. When Fr = 0.2, the ice blocks are significantly displaced as in Fig. 13(c), and R_{ice} is dramatically increased. For h = 48 mm, the observed speed dependence is similar to that of h = 36 mm, as shown in Fig. 14.

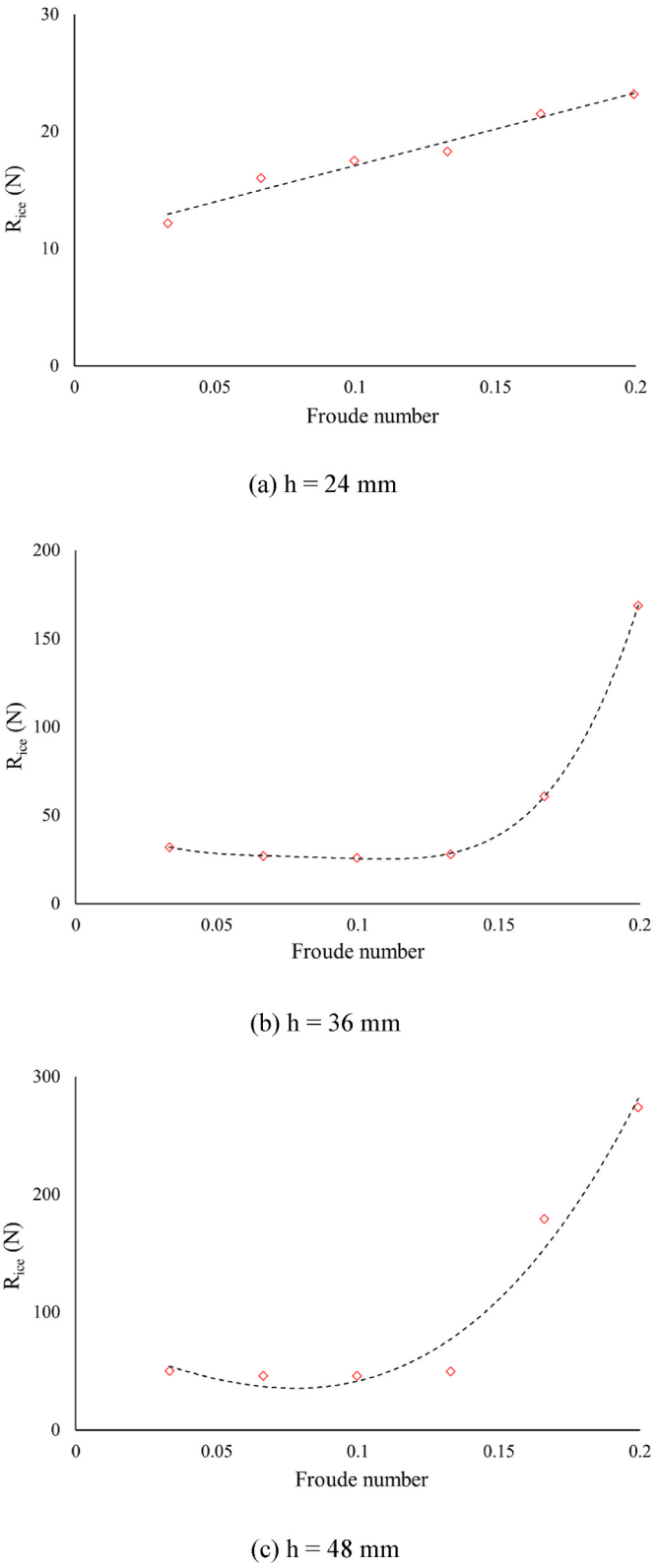

Fig. 11. Computational pre-sawn ice resistance against ship speed.

4.2. Discussion on speed dependence

Overall, the results reveal two mechanisms through which ship speed affects ice resistance. The first is the coverage of ice blocks on the ship

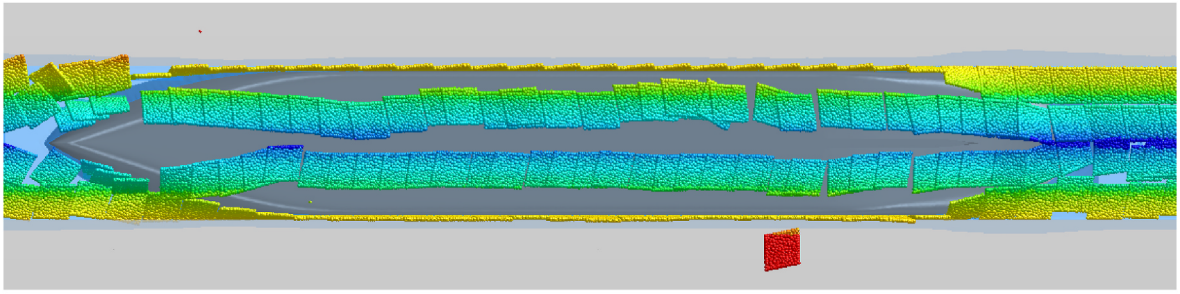

(a) Fr = 0.066, NSIB = 60, R_{ice} = 16 N

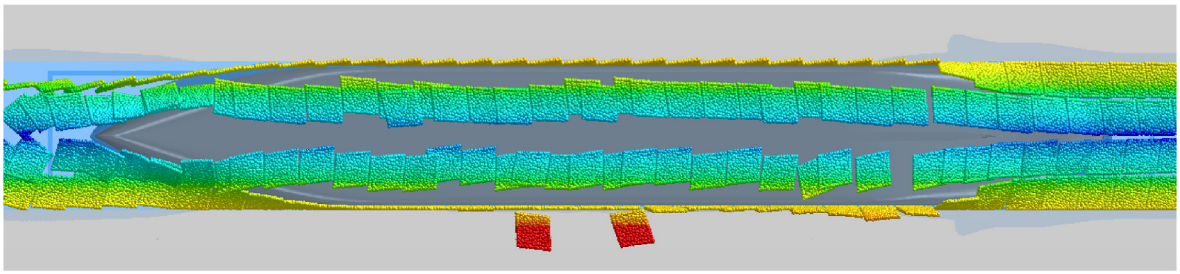

(b) Fr = 0.133, NSIB = 60, R_{ice} = 18.3 N

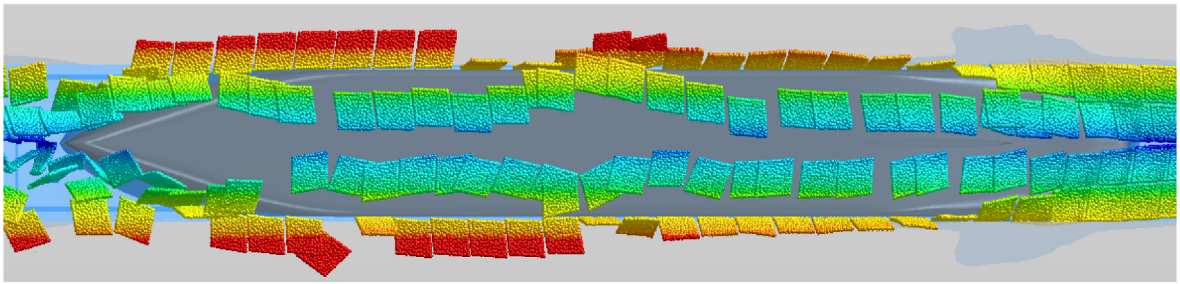

(c) Fr = 0.2, NSIB = 50, R_{ice} = 23.2 N

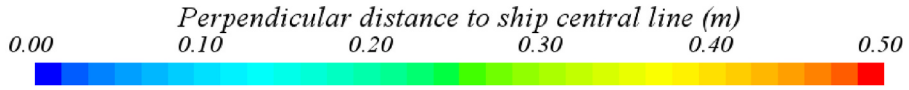

Fig. 12. Fish views of simulations with different ship velocities (h = 24 mm). The contour indicates the relative location of each ice block to the ship's central line, which is applicable for all following pictures.

underwater, and the second is the movement of ice blocks due to the contact with the ship. The former contributes to R_F while the latter relates to R_C. It is found that R_F decreases whilst R_C increases with increasing ship speed. The decrease in R_F is due to a higher ship speed that tends to reduce the amount of submerged ice. Thicker ice blocks are easier to overlap when the ship speed is low, which increases NSIB and provides additional R_F. The increase in R_C results from a higher-speed ship accelerating and displacing ice blocks from their initial locations. For thicker ice, R_C may change inconspicuously in the low ship-speed range, where ice blocks uniformly distribute underneath the ship and varying ship speed is not sufficient to break the pattern. A dramatic increase in R_C occurs when ship speed is high enough to break the pattern and the distribution of ice blocks becomes chaotic, which is particularly influential for thicker ice. Since the kinetic energy an ice block gains is proportional to the square of its speed, the resistance R_C becomes more sensitive to speed change in the high-speed regime and therefore dominates the total resistance. In the low-speed regime, the change in R_F and R_C offsets each other so the overall resistance change is not explicit. The nonlinearity of R_C is affected by ice thickness as thinner ice is earlier to be moved.

Hydrodynamics can also influence the speed dependence. Fig. 15 presents the water speed vectors in front of the ship. It can be seen that the maximum water speed in front of the ship is around half of the ship advancing speed, whilst the hydrodynamic intensity is low for Fr = 0.066 and 0.133 but relatively high for Fr = 0.2. However, in Figs. 12–14, it can be seen that the ice pattern in front of the ship is almost same for the three ship speeds, so the water flow is not strong enough to dictate the floe motions. Therefore, the hydrodynamic effect in the pre-sawn ice case is minimal due to the large size of ice floes. It can be inferred that hydrodynamics will be significant for small ice floes, such as pancake ice (Huang et al., 2020).

The strong non-linearity of speed dependence has been reported in the literature. van der Werff et al. (2015) conducted experiments using artificial pre-sawn ice, and the results (see their Fig. 13) showed high similarity to the resistance curves of h = 36 mm and h = 48 mm in the present work - Fig. 11(b) and (c). The non-distinctive speed dependence in low/middle-speed ranges has also appeared in many previous laboratory and field measurements of ships in broken ice fields, such as

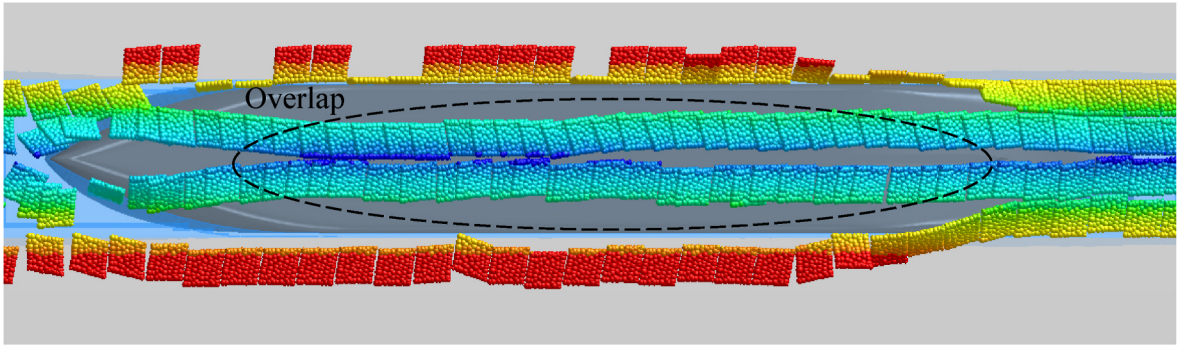

(a) Fr = 0.066, NSIB = 72, R_{ice} = 26.9 N

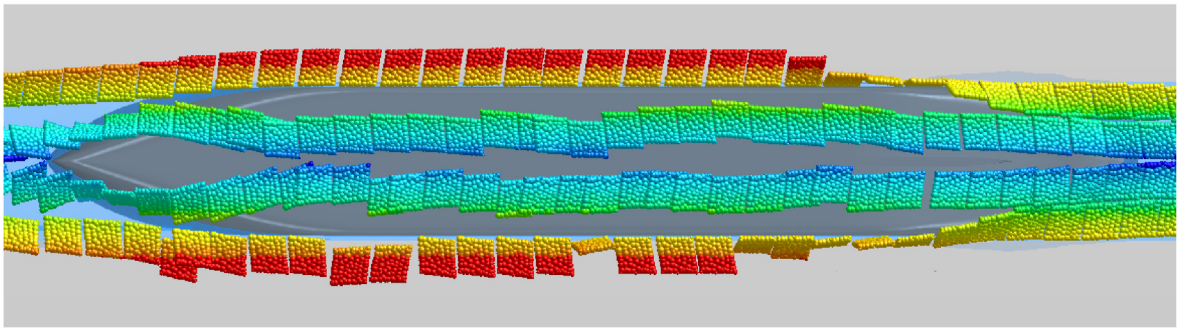

(b) Fr = 0.133, NSIB = 64, R_{ice} = 27.9 N

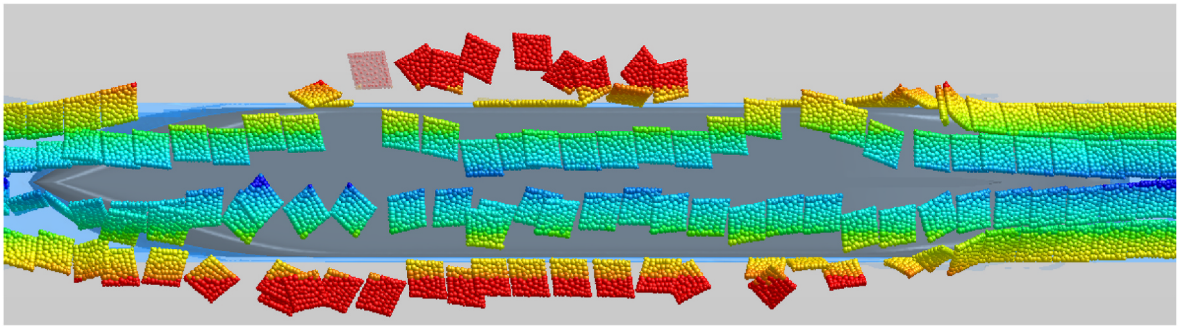

(c) Fr = 0.2, NSIB = 56, R_{ice} = 168.4 N

Fig. 13. Fish views of simulations with different ship velocities (h = 36 mm).

(Jones, 2004; Jeong et al., 2010; Suyuthi et al., 2011; Huang et al., 2016; Hu and Zhou, 2016; Yang et al., 2021). Nonetheless, these previous studies did not break the conventional assumption that ice resistance linearly changes ship speed for any speed range. This is because the measured data of all speed conditions were usually fit together - dramatic increase trends in high-speed conditions appear to override the non-distinctive speed dependence in low/middle-speed ranges.

As this paper specifically looks into how speed affects resistance by the ice distribution and movement as the result of ship advancement. There are still some other mechanisms that could affect the speed dependence, such as the size changing of ice pieces in icebreaking processes with varying V, and the ventilation and dynamic pressure effects as reviewed earlier, which are out of the scope of this paper. The main contribution of this work is demonstrating the advanced CFD + DEM approach through the pre-sawn ice case and the explanation of how speed affects ice resistance through ice piece distribution and movement, which provides new insight into the mechanism of speed dependence of ice resistance. The speed dependence of the overall ice resistance in reality is a mixture of different mechanisms, which includes but is not limited to the effects revealed here.

4.3. Future work

Certain future work could be done to complement the findings in this paper. From a simulation perspective, different hull forms can be used to investigate how the ice coverage differs and whether the mode of speed dependence changes. From an experimental perspective, underwater cameras may be installed to confirm the role of ice patterns underneath a ship. For example, image analysis tools similar to that adopted by Myland and Ehlers (2020) can be deployed to provide quantitative analyses of the ice distribution. Moreover, innovative sensors to track the motion of ice pieces could be particularly useful.

It is noteworthy that the multiple-particle DEM approach can enable an ice block to break up, by specifying maximum tensile strength and maximum shear strength between particles. During a simulation, the solver calculates the tensile and shear stresses between particles; if the stress exceeds its maximum limit, the bond breaks and the particles separate. This may be particularly useful to model phenomena

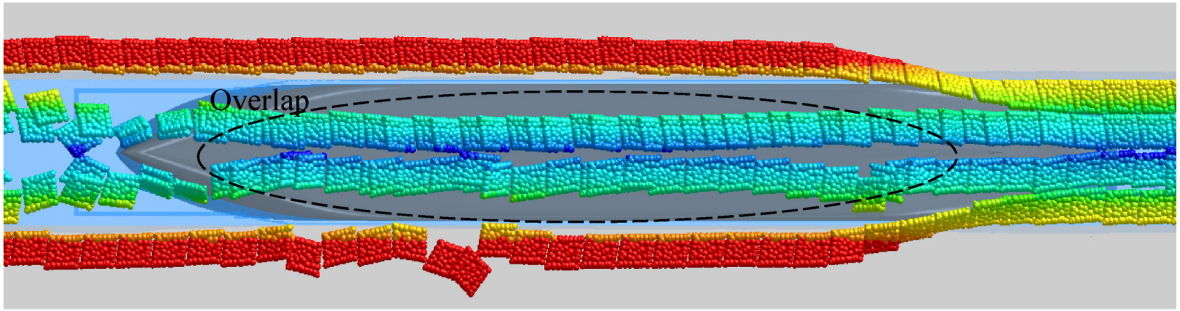

(a) Fr = 0.066, NSIB = 72, R_{ice} = 45.8 N

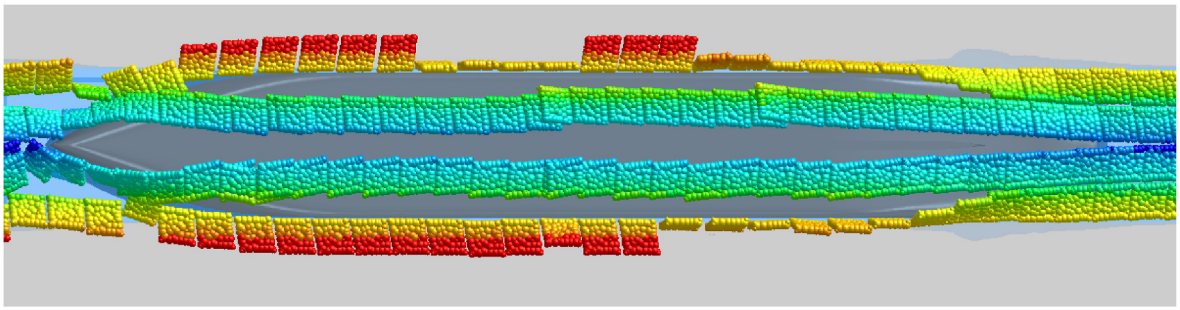

(b) Fr = 0.133, NSIB = 64, R_{ice} = 49.8 N

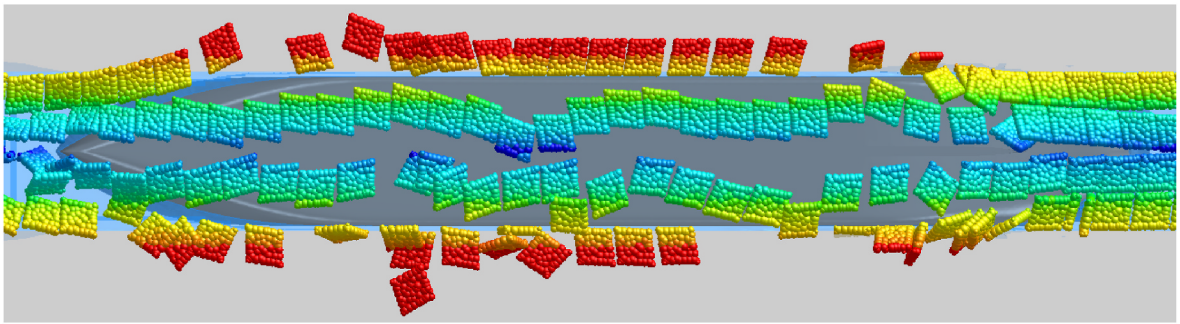

(c) Fr = 0.2, NSIB = 56, R_{ice} = 274 N

Fig. 14. Fish views of simulations with different ship velocities (h = 48 mm).

containing ice breakups, such as a ship operating in level ice, large ice floes, and ice ridges (Ni et al., 2020; Chai et al., 2020; Li et al., 2021; Jeong et al., 2021). The maximum limit of stresses can also be set as a function of load and loading time, which is useful when the bond can be damaged under a continuous load (brittle fracture growth), e.g. ice in waves (Dolatshah et al., 2018; Huang et al., 2019; Passerotti et al., 2021; He et al., 2022). High-fidelity modelling of ice breakup is significantly missing in existing literature, thus the present CFD + DEM approach can be used for a substantial area of future work (Li and Huang, 2022).

5. Conclusions

This paper presented an advanced CFD + DEM model for simulating a ship's pre-sawn ice tests. A multiple-particle DEM approach was introduced to simulate discrete ice blocks, which significantly improved the solution of ice motions. Parallel experiments were conducted to prove the model's accuracy. Upon validating the developed model, computational investigations on a ship's interaction with pre-sawn ice were conducted.

This research aimed at exploring the speed dependence of the submerged and clearing components of ice resistance, as extensive previous measurements indicated complex R_{ice} variation against ship speed but the underlying mechanism had not been clarified. The present simulations complement experimental eyes by providing fish views to observe the underwater ice patterns at different ship speed and ice thickness conditions, which corroborated that R_{ice} does not always linearly increase with increasing ship speed, especially for lower ship speed and thicker ice conditions.

The simulations identified two significant sources of the speed dependence: (a) the mass of submerged ice, and (b) the kinetic energy required for displacing broken ice. The findings bring new insights to the mechanism of the speed effect on ice resistance and suggest separating the speed dependence into low-speed and high-speed regimes. This will potentially help improve relevant empirical equations, and facilitate ship design, operational strategies and maritime management in polar regions.

CRediT authorship contribution statement

Luofeng Huang: Conceptualization, Methodology, Software, Validation, Formal analysis, Resources, Visualization, Investigation, Writing – original draft. **Fang Li:** Conceptualization, Methodology, Validation,

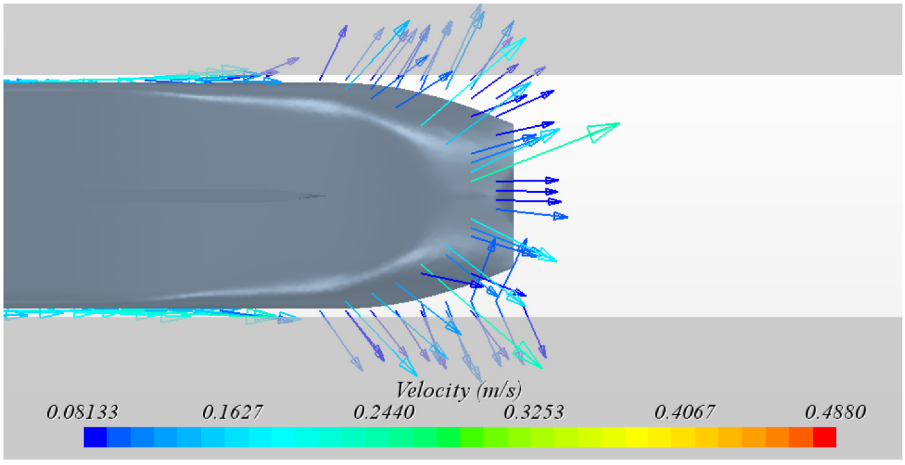

(a) Fr = 0.066, V = 0. 488 m/s

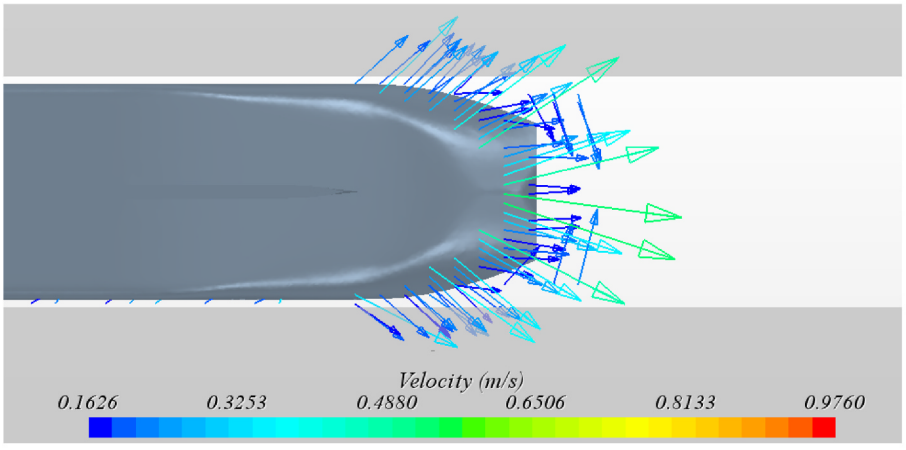

(b) Fr = 0.133, V = 0.976 m/s

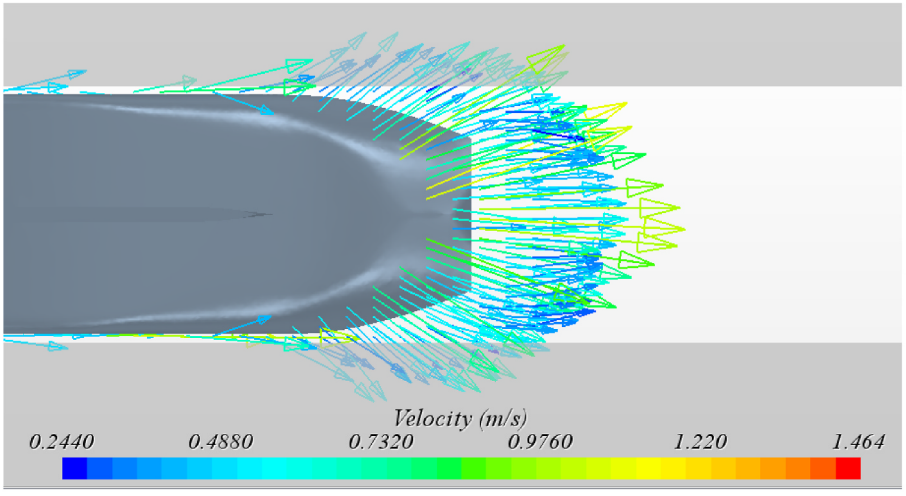

(c) Fr = 0.2, V = 1.464 m/s

Fig. 15. Demonstration of hydrodynamics in front of the ship.

Formal analysis, Resources, Investigation, Writing – original draft. **Minghao Li:** Methodology, Software, Visualization. **Danial Khojasteh:** Formal analysis, Investigation, Writing – review & editing. **Zhenhua Luo:** Supervision, Resources, Writing – review & editing. **Pentti Kujala:** Supervision, Resources, Writing – review & editing.

Declaration of competing interest

The authors declare that they have no known competing financial interests or personal relationships that could have appeared to influence the work reported in this paper.

Data availability

All data underlying the results are available as part of the article and no additional source data are required.

References

Baran, O., 2012. Discrete element method in STAR CCM+. In: STAR Japanese Conference.

Chai, W., Leira, B.J., Naess, A., Høyland, K., Ehlers, S., 2020. Development of environmental contours for first-year ice ridge statistics. Struct. Saf. 87, 101996.

Cundall, P.A., Strack, O.D., 1979. A discrete numerical model for granular assemblies. Geotechnique 29, 47–65.

Dolatshah, A., Nelli, F., Bennetts, L.G., Alberello, A., Meylan, M.H., Monty, J.P., Toffoli, A., 2018. Hydroelastic interactions between water waves and floating freshwater ice. Phys. Fluids 30, 091702.

Enkvist, E., 1972. On the Ice Resistance Encountered by Ships Operating in the Continuous Mode of Icebreaking. Swedish Academy of Engineering Sciences, Finland.

Gutiérrez-Romero, J.E., Ruiz-Capel, S., Esteve-Pérez, J., Zamora-Parra, B., Luna-Abad, J. P., 2022. Methodology based on photogrammetry for testing ship-block resistance in traditional towing tanks: observations and benchmark data. J. Mar. Sci. Eng. 10, 246.

He, K., Ni, B., Xu, X., Wei, H., Xue, Y., 2022. Numerical simulation on the breakup of an ice sheet induced by regular incident waves. Appl. Ocean Res. 120, 103024.

Hirt, C.W., Nichols, B.D., 1981. Volume of fluid (VOF) method for the dynamics of free boundaries. J. Comput. Phys. 39, 201–225.

Hu, J., Zhou, L., 2016. Further study on level ice resistance and channel resistance for an icebreaking vessel. Int. J. Nav. Archit. Ocean Eng. 8, 169–176.

Huang, L., Igrec, B., Thomas, G., 2022. New tools to generate realistic ice floe fields for computational models. J. Offshore Mech. Arctic Eng. 144 https://doi.org/10.1115/1.4054658.

Huang, L., Li, M., Romu, T., Dolatshah, A., Thomas, G., 2021a. Simulation of a ship operating in an open-water ice channel. Ships Offshore Struct. 16, 353–362. https://doi.org/10.1080/17445302.2020.1729595.

Huang, L., Li, Z., Ryan, C., Ringsberg, J.W., Pena, B., Li, M., Ding, L., Thomas, G., 2021b. Ship resistance when operating in floating ice floes: derivation, validation, and application of an empirical equation. Mar. Struct. 79, 103057.

Huang, L., Ren, K., Li, M., Tuković, Ž., Cardiff, P., Thomas, G., 2019. Fluid-structure interaction of a large ice sheet in waves. Ocean Eng. 182, 102–111.

Huang, L., Tavakoli, S., Li, M., Dolatshah, A., Pena, B., Ding, B., Dashtimanesh, A., 2021c. CFD analyses on the water entry process of a freefall lifeboat. Ocean Eng. 232, 109115.

Huang, L., Tuhkuri, J., Igrec, B., Li, M., Stagonas, D., Toffoli, A., Cardiff, P., Thomas, G., 2020. Ship resistance when operating in floating ice floes: a combined CFD&DEM approach. Mar. Struct. 74, 102817.

Huang, Y., Sun, J., Ji, S., Tian, Y., 2016. Experimental study on the resistance of a transport ship navigating in level ice. J. Mar. Sci. Appl. 15, 105–111.

ITTC, 2017. General Guidance and Introduction to Ice Model Test. ITTC Report.

ITTC, 2014. Guidelines: Practical Guidelines for Ship CFD Applications. ITTC Report.

ITTC, 2002. Testing and Extrapolation Methods: Ice Testing: Resistance Test in Level Ice. ITTC Report.

Jeong, S.-Y., Choi, K., Kang, K.-J., Ha, J.-S., 2017. Prediction of ship resistance in level ice based on empirical approach. Int. J. Nav. Archit. Ocean Eng. 9, 613–623.

Jeong, S.-Y., Choi, K., Kim, H.-S., 2021. Investigation of ship resistance characteristics under pack ice conditions. Ocean Eng. 219, 108264.

Jeong, S.-Y., Lee, C.-J., Cho, S.-R., 2010. Ice resistance prediction for standard icebreaker model ship. In: The Twentieth International Offshore and Polar Engineering Conference. OnePetro.

Johnson, K.L., Johnson, K.L., 1987. Contact Mechanics. Cambridge University Press, Cambridge, UK.

Jones, S.J., 2004. Ships in ice - a review. In: 25th Symposium on Naval Hydrodynamics. National Academies Press, Washington D.C., US.

Juva, M., Riska, K., 2002. On the power requirement in the Finnish-Swedish ice class rules. Winter Navig. Res. Board, Res. Rpt 53.

Kämäräinen, J., 2007. Theoretical Investigation on the Effect of Fluid Flow between the Hull of a Ship and Ice Floes on Ice Resistance in Level Ice (PhD Thesis). Helsinki University of Technology.

Kämäräinen, J., 1993. Evaluation of Ship Ice Resistance Calculation Methods (Licentiate's Thesis). Helsinki University of Technology, Faculty of Mechanical Engineering.

Konno, A., Mizuki, T., 2006. Numerical simulation of pre-sawn ice test of model icebreaker using physically based modeling. In: The 18th IAHR International Symposium on Ice. Hokkaido University, Sapporo, Japan.

Li, F., Huang, L., 2022. A review of computational simulation methods for a ship advancing in broken ice. J. Mar. Sci. Eng. 10, 165. https://doi.org/10.3390/jmse10020165.

Li, F., Suominen, M., Kujala, P., 2021. Ship performance in ice channels narrower than ship beam: model test and numerical investigation. Ocean Eng. 240, 109922.

Lindqvist, G., 1989. Straightforward Method for Calculation of Ice Resistance of Ships. The 10th international conference on Port and Ocean Engineering under Arctic Conditions. POAC89.

Lu, W., Løset, S., Lubbad, R., 2012. Ventilation and backfill effect during ice-structure interactions. In: The 21st IAHR International Symposium on Ice. Dalian, China, pp. 826–841.

Luo, W., Jiang, D., Wu, T., Guo, C., Wang, C., Deng, R., Dai, S., 2020. Numerical simulation of an ice-strengthened bulk carrier in brash ice channel. Ocean Eng. 196, 106830.

Menter, F., 1993. Zonal two equation kw turbulence models for aerodynamic flows. In: 23rd Fluid Dynamics, Plasmadynamics, and Lasers Conference, p. 2906.

Mucha, P., 2019. Fully-coupled CFD-DEM for simulations of ships advancing through brash ice. In: SNAME Maritime Convention. The Society of Naval Architects and Marine Engineers.

Myland, D., Ehlers, S., 2020. Model scale investigation of aspects influencing the ice resistance of ships sailing ahead in level ice. Ship Technol. Res. 67, 26–36.

Ni, B.-Y., Chen, Z.-W., Zhong, K., Li, X.-A., Xue, Y.-Z., 2020. Numerical simulation of a polar ship moving in level ice based on a one-way coupling method. J. Mar. Sci. Eng. 8, 692.

Passerotti, G., Bennetts, L.G., Alberello, A., Puolakka, O., Dolatshah, A., Monbaliu, J., Toffoli, A., 2021. Interactions between Irregular Wave Fields and Sea Ice: A Physical Model for Wave Attenuation and Ice Break up arXiv preprint arXiv:2110.12659.

Pena, B., Huang, L., 2021. A review on the turbulence modelling strategy for ship hydrodynamic simulations. Ocean Eng. 241, 110082.

Puntigliano Etchart, F.M., 2003. Experimental and numerical research on the interaction between ice flows and a ship's hull during icebreaking. TU Hamburg–Harburg, Schriftenreihe Schiffbau, Bericht Nr 622. September 2003.

Sawamura, J., Kioka, S., Konno, A., 2015. Experimental and numerical investigation on ice submerging for icebreaker with 2D model test using synthetic ice. In: Proceedings of the International Conference on Port and Ocean Engineering under Arctic Conditions. POAC15.

Seo, D.C., Wang, J., 2021. Numerical simulation of model test in pre-sawn ice by CFD-DEM coupled method. In: International Conference on Offshore Mechanics and Arctic Engineering. American Society of Mechanical Engineers. V007T07A011.

Spencer, D., Jones, S.J., 2001. Model-scale/full-scale correlation in open water and ice for Canadian Coast Guard "R-Class" icebreakers. J. Ship Res. 45, 249–261.

Suyuthi, A., Leira, B.J., Riska, K., 2011. Full scale measurement on level ice resistance of icebreaker. In: International Conference on Offshore Mechanics and Arctic Engineering, pp. 983–989.

Tan, X., Riska, K., Moan, T., 2014. Effect of dynamic bending of level ice on ship's continuous-mode icebreaking. Cold Reg. Sci. Technol. 106, 82–95.

Terziev, M., Tezdogan, T., Incecik, A., 2019. Application of eddy-viscosity turbulence models to problems in ship hydrodynamics. Ships Offshore Struct. 1–24.

Valanto, P., 2001. The resistance of ships in level ice. SNAME Trans. 109, 53–83.

Valanto, P.U., 1989. Experimental and Theoretical Investigation of the Icebreaking Cycle in Two Dimensions (PhD Thesis). University of California, Berkeley.

van der Werff, S., Brouwer, J., Hagesteijn, G., 2015. Ship resistance validation using artificial ice. In: International Conference on Offshore Mechanics and Arctic Engineering. American Society of Mechanical Engineers. V008T07A043.

Versteeg, H.K., Malalasekera, W., 2007. An Introduction to Computational Fluid Dynamics: the Finite Volume Method. Pearson Education, London, UK.

Yang, B., Sun, Z., Zhang, G., Wang, Q., Zong, Z., Li, Z., 2021. Numerical estimation of ship resistance in broken ice and investigation on the effect of floe geometry. Mar. Struct. 75, 102867.

Zhang, J., Zhang, Y., Shang, Y., Jin, Q., Zhang, L., 2022. CFD-DEM based full-scale ship-ice interaction research under FSICR ice condition in restricted brash ice channel. Cold Reg. Sci. Technol. 194, 103454.

Zhou, L., Riska, K., und Polach, R. von B., Moan, T., Su, B., 2013. Experiments on level ice loading on an icebreaking tanker with different ice drift angles. Cold Reg. Sci. Technol. 85, 79–93.

Zong, Z., Yang, B.Y., Sun, Z., Zhang, G.Y., 2020. Experimental study of ship resistance in artificial ice floes. Cold Reg. Sci. Technol. 176, 103102.